



Delivery of CW laser power up to 300 watts at 1080 nm by an uncooled low-loss anti-resonant hollow-core fiber

XINYUE ZHU,^{1,2} DAKUN WU,^{3,7}  YAZHOU WANG,^{2,4} FEI YU,^{2,3,8}  QIURUI LI,⁵ YUNFENG QI,⁵ JONATHAN KNIGHT,⁶  SHUFEN CHEN,¹ AND LILI HU^{2,3} 

¹School of Optics and Photonics, Beijing Institute of Technology, Beijing 100081, China

²Key Laboratory of Materials for High Power Laser, Shanghai Institute of Optics and Fine Mechanics, Chinese Academy of Sciences, Shanghai 201800, China

³Hangzhou Institute for Advanced Study, UCAS, Hangzhou 310024, China

⁴Center of Materials Science and Optoelectronics Engineering, University of Chinese Academy of Sciences, Beijing 100049, China

⁵Shanghai Key Laboratory of All Solid-State Laser and Applied Techniques, Shanghai Institute of Optics and Fine Mechanics, Chinese Academy of Sciences, Shanghai 201800, China

⁶Centre for Photonics and Photonic Materials, Department of Physics, University of Bath, Claverton Down, Bath, BA2 7AY, United Kingdom

⁷wudakun@ucas.ac.cn

⁸yufei@siom.ac.cn

Abstract: In this paper, we report the use of a 3-meter low-loss anti-resonant hollow-core fiber (AR-HCF) to deliver up to 300 W continuous-wave laser power at 1080 nm wavelength from a commercial fiber laser source. A near-diffraction-limited beam is measured at the output of the AR-HCF and no damage to the uncooled AR-HCF is observed for several hours of laser delivery operation. The limit of AR-HCF coupling efficiency and laser-induced thermal effects that were observed in our experiment are also discussed.

© 2021 Optical Society of America under the terms of the [OSA Open Access Publishing Agreement](#)

1. Introduction

Demand for flexible laser power delivery using optical fiber has been growing with the rapid development of high-power laser sources which could find extensive applications in micro-machining, laser surgery, defense technology and other applications [1–3]. The power handling ability of conventional optical fiber is determined by its laser power damage threshold, nonlinear optical effects and thermal induced modal degradation, all of which are ultimately constrained by the glass core. Hollow-core fibers (HCFs) confine the light in the hole and provide a nearly free-space propagation environment with a much higher damage threshold, lower optical nonlinearity, and lower waveguide dispersion. These unique advantages give HCFs the potential to outperform the solid-core fiber [4], particularly in high-power laser delivery.

Thanks to the concept of microstructured design, HCFs can have attenuation as low as tens of dB/km or less, and therefore HCF-based high-power laser delivery is becoming practical. Photonic-bandgap hollow-core fiber (PBG-HCF) (the first kind of low-loss HCF) has been used to deliver laser pulses by taking advantage of its low dispersion and low optical nonlinearity [5–7]. In 2016, a PBG-HCF successfully delivered 76 W average power picosecond laser pulses at 1032 nm, with 1.9 μ J pulse energy of 22 ps pulse [8]. PBG-HCFs were also used to transmit continuous wave (CW) laser [9,10] and up to 100 W CW laser power delivery was successfully demonstrated [11].

Kagome-HCF, a different type of microstructured HCF, has been widely used in ultrafast pulse compression, and high power/high field laser transmission [12–17]. In 2014, pulsed laser of

18 μJ and 740 fs, with 118 W average power was coupled into a Kagome-HCF filled with 13 bar of argon for spectral broadening and compression [18]. For few-cycle laser pulse transmission, undistorted 10 fs and 6.6 nJ pulses were launched into a 1 m long Kagome HCFs with 80% transmission efficiency reported [19]. S. Hädrich et al. [20] delivered few-cycle laser with an average power up to 900 W, using a Kagome HCF that was cooled in the experiment and the laser delivery operation lasted for about 20 minutes in experiment.

Inspired by the concept of negative-curvature core boundary [21], the negative-curvature anti-resonant hollow-core fiber (AR-HCF) was first proposed in 2011 [22]. AR-HCFs are known for their simplified cladding and the large hollow core, which can efficiently confine the light with low loss [23–25]. In AR-HCF, light is guided in the central hollow core by taking advantage of the ultrathin negative-curvature core wall ranging from hundreds of nanometers to a few micrometers generally [26–28] which works in a way analogous to a Fabry-Perot resonator. Additionally, the high order modes (HOMs) in the core would be effectively filtered by coupling with cladding modes when the phase matching condition is satisfied so that AR-HCF could possibly achieve a quasi-single-mode guidance [29]. Besides, comparing with PBG-HCF and Kagome-HCF, AR-HCFs have the largest core diameter for the same spectral transmission window which is key for leakage loss reduction and meanwhile brings down the power fraction of mode field distributed in the host material of cladding [30,31], helping to boost the laser damage threshold significantly. It is noted that the flexibility of AR-HCF would be hindered at some extent by its bending sensitivity and a systematic experimental characterization is found in [32]. So far, pulsed laser delivery using AR-HCF has been extensively studied, most at visible and near-infrared wavelengths [33–39]. In the visible spectral region, AR-HCF was used to deliver a high energy pulsed laser with around 0.57 mJ (10.4 kW peak power) and 30 μJ (5 MW peak power) pulse energies at 532 nm and 515 nm respectively [40]. As for the near-infrared, an average laser power of over 70 W at 1032 nm with 22 ps pulse duration and 10 MHz repetition rate was transmitted in AR-HCF [41]. Meanwhile, ultraviolet (UV) pulse delivery by AR-HCF has also been demonstrated [42,43]. Yu et al. reported solarization-free UV pulse transmission by AR-HCF, delivering 17 ns laser pulses at 266 nm at 30 kHz repetition rate [43].

In this paper, we successfully demonstrate 300 W CW laser power delivery over 3 m AR-HCF fiber length at 1080 nm. No fiber damage is observed for 400 W incident power, limited by the maximum output of our fiber laser source. We experimentally characterize the temporal stability of laser transmission in AR-HCF, beam quality and numerical aperture at the AR-HCF output as function of incident power. Optimization of free-space laser beam coupling with AR-HCF is modelled and discussed.

2. AR-HCF for high-power laser delivery

The AR-HCF used in this paper is fabricated by stack-and-draw technique, starting with Heraeus F300 fused silica tubes. It consists of a ring of seven capillaries forming the cladding (inset of Fig. 1), with a core diameter of about 35 μm and an average capillary inner diameter of 17 μm . The 7-capillary cladding design of AR-HCF is preferred in the fabrication for optimized balance between the single-mode guidance [44] and minimization of cladding gaps for lower leakage loss [45]. The thickness of negative-curvature core wall is about 355 nm on average, indicating the first and second resonance wavelengths around 750 nm and 384 nm wavelengths, respectively. The attenuation of the AR-HCF measured by the cut-back method is shown in Fig. 1 and 0.05 dB/m is obtained at 1080 nm wavelength.

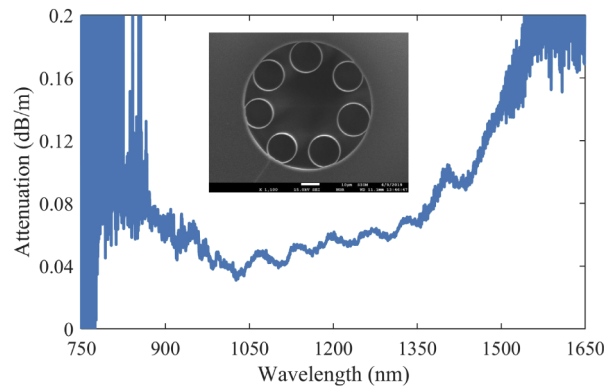


Fig. 1. The measured attenuation of the AR-HCF by a cut-back from 132 m to 12 m. Inset: SEM picture of AR-HCF. The core diameter is about 35 μm .

3. Experiment of high-power laser delivery by AR-HCF

3.1. Experimental setup

Figure 2 shows our CW laser delivery experiment setup. 3 meters AR-HCF, which is relatively suitable for high power delivery, was loosely rewound on a steel plate in a circle with a radius of about 50 cm to be confident that we would not introduce resonant bend loss [32]. Such large loop diameter is preferred to avoid the possible burning of fiber coating by bend induced laser power leakage which would severely damage AR-HCF. It is noted that the acrylic coating was not stripped off from AR-HCF except at the two fiber ends. The fiber was not cooled during the experiment.

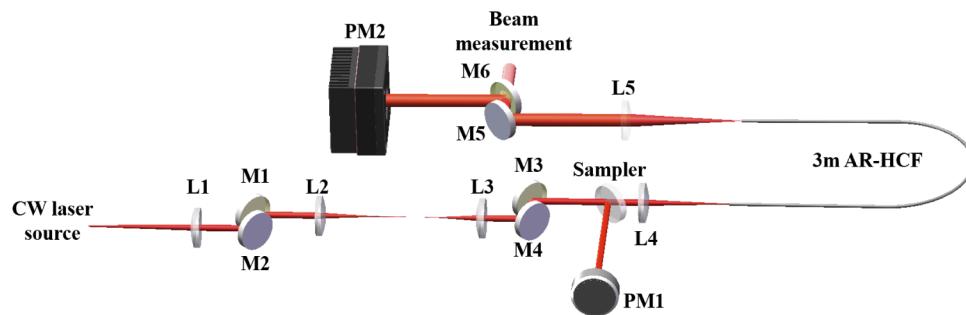


Fig. 2. Schematic of laser delivery setup: L1, L2, L3, L4 are coated aspherical lens with $f_1 = 100 \text{ mm}$, $f_2 = 150 \text{ mm}$, $f_3 = 120 \text{ mm}$, $f_4 = 100 \text{ mm}$; M1, M2, M3, M4, M5 are dielectric mirrors which reflect $> 99.5\%$; M6 is a back polished mirror used as a sampler (transmittance $<< 1\%$); Another sampler (99:1) is used to monitor the power of laser source and calibrate the incident power at the input end of the AR-HCF in real time. PM1, PM2 are power meters. AR-HCF is mounted on a silica V groove loaded on a XYZ stages. No cooling method is applied.

An industrial CW fiber laser (Feibo YDFL-500-QCW) used as the source provides a maximum power up to 400 W at 1080 nm. M^2 measurement of laser output is shown in Fig. 4. The laser beam leaving the end cap is 5 mm in diameter according to the specification. A 4- f lens system is designed and used to scale the laser beam and couple with AR-HCF.

In the experiment, about 15 cm coating was stripped off of the AR-HCF ends to avoid burning damage caused by the uncoupled laser power. The bare fiber end was mounted on a silica

V-groove on a XYZ stage (Thorlabs MAX313D). A sampler is used to monitor the incident power and calibrate the coupling efficiency in real time. At the AR-HCF output, the delivered laser power and beam quality are measured at the same time after the collimating lens (L5).

3.2. Characterization of laser power delivery

Figure 3 shows the measured laser power output after transmission by 3 m AR-HCF and its corresponding coupling efficiency η excluding the fiber attenuation, defined by

$$\eta = \frac{P_{out}}{P_{in}} \cdot 10^{\frac{aL}{10}} \quad (1)$$

where P_{out} denotes the output power measured after L5 while P_{in} the input power measured after L4, a the measured fiber attenuation (with unit of dB/m) and L the transmission length of fiber.

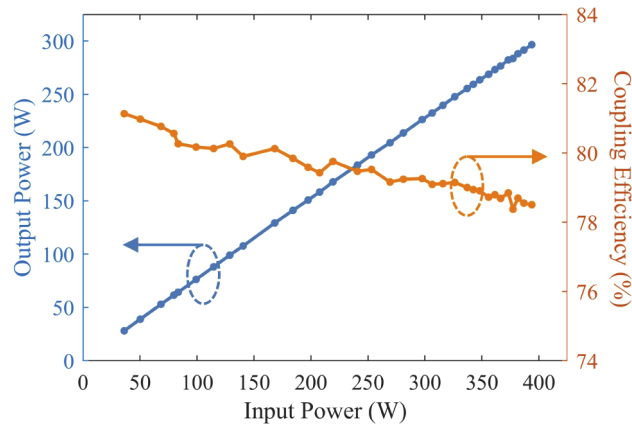


Fig. 3. Measured output power and coupling efficiency as function of incident laser power. The coupling efficiency is defined by Eq. (1).

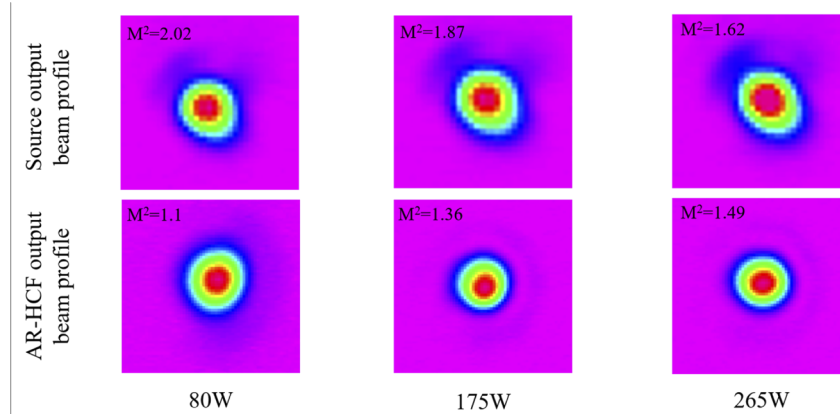


Fig. 4. Beam profiles and corresponding M^2 factors of the incident laser beam (upper row) and output at the end of AR-HCF (lower row) for different laser powers.

We demonstrate the delivery of a maximum 300 W laser power measured at AR-HCF output for 1 hour, while over ten hours' delivery was demonstrated without observing fiber damage

or coating burning for incident powers ranging from 50 W to 280 W. In the experiment, the optimized coupling efficiency was 81% for low incident powers below 100 W and gradually dropped to around 78.6% at 400 W input power.

When the laser was switched on at high power, a noticeable thermal drifting of XYZ stage was observed due to the heating by the uncoupled optical power. Such misalignment of the coupling condition could be compensated by transverse manual adjustment of the XYZ stage. In experiment we also found that with increasing incident power, the focal position moved back toward the lens which required the longitudinal manual adjustment of XYZ stage. However, these manual adjustments failed to maintain optimized coupling efficiency for high incident power. We attribute the degradation of coupling efficiency to the thermal induced lensing effects giving rise to a smaller beam size at the focus plane after L4 as discussed later.

3.3. Output beam quality from AR-HCF

The delivered laser beam profile at the AR-HCF output was characterized for different incident powers by measuring the M^2 factor as shown in Fig. 4. Back-polished dielectric mirrors are used to attenuate the laser beam before the beam profiler (HP-LQM, Prime). Although the incident beam quality becomes slightly better as the power increases, M^2 is found always above 1.5 which makes the high coupling efficiency a challenge (as discussed in Section 4.1). The numerical aperture of delivered beam is measured as 0.0326 at 30 W incident power, and rises slightly to 0.0377 at 220 W.

Our simulation shows that the fundamental mode of AR-HCF has an average leakage loss of 0.034 dB/m at 1080 nm while LP_{11} -like mode 0.308 dB/m, corresponding to a HOM extinction ratio of about 9. Excited HOMs associated with higher losses dissipate in AR-HCF faster which assists the modal filtering effect in the laser delivery. As shown in Fig. 4, the delivered laser beam out of AR-HCF presents a near diffraction limited beam quality at low incident power below 100 W and slightly degrades for higher power implying the rising of HOMs in the transmission.

3.4. Temporal stability of laser power delivery by AR-HCF

Figure 5(a) records the temporal measurement of coupling efficiency of AR-HCF for different incident power when no manual adjustment was applied for coupling optimization. The coupling efficiency was found to stay stable for the first ten to fifteen minutes for both low and high incident power and then decrease at a different rate depending on the heat accumulation. We point out

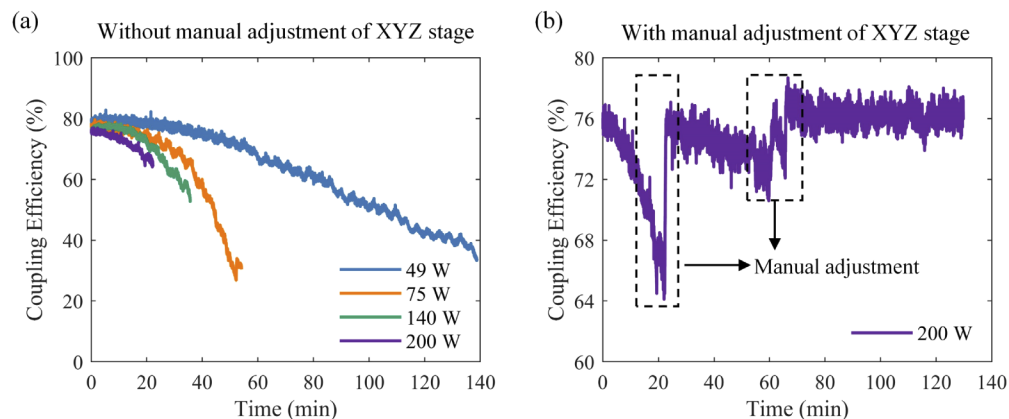


Fig. 5. Temporal measurement: (a) coupling efficiency without adjusting the XYZ stage for different incident power; (b) coupling efficiency for 200 W input power, with manual adjustment of XYZ stage at 20 and 60 minutes, respectively.

that such degraded coupling efficiency would be recovered by manually adjusting the XYZ stages. Even at high incident power, after the manual adjustment and when a thermal equilibrium status was reached, the laser delivery by AR-HCF could become stable for a period of an hour or more as shown in Fig. 5(b).

A longer time demonstration of high-power laser delivery by AR-HCF was unfortunately limited by the performance of our current laser source. As Fig. 5(b) implies, when XYZ stage and lenses reach the thermal equilibrium condition, high-power laser delivery by AR-HCF is possible to achieve for much long time, which will be explored in our future work.

4. Discussion

4.1. Towards an improved coupling efficiency

In our experiment, we managed to achieve only 81% coupling efficiency from the free space laser beam to AR-HCF while 92% was reported in [38]. We set up an intermodal coupling model of free-space beam with AR-HCF and numerically calculate the coupling efficiency by using the finite element software COMSOL.

The coupling efficiency η defined as the ratio of power coupled into modes of AR-HCF over the total incident beam power at the end, is given by [46]

$$\eta = \frac{\left| \iint E_i(x, y) E_f^*(x, y) dx dy \right|^2}{\left[\iint |E_i(x, y)|^2 dx dy \right] \left[\iint |E_f(x, y)|^2 dx dy \right]} \quad (2)$$

where E_i denotes the incident optical field in the fiber end-face plane while E_f the modal profile of AR-HCF. Our AR-HCF allows HOMs with relatively low loss. In the model, we take the fundamental mode and LP₁₁-like mode of AR-HCF into account only.

To obtain the modal field distributions of AR-HCF, we reconstructed the CAD model of AR-HCF from its SEM picture and simulated it using COMSOL. We approximately rebuild the incident laser beam field by linearly scaling the linear polarized (LP) mode expressions of the pigtail fiber of laser (Nufern LMA-GDF-20/400, core radius of 10 μm and NA of 0.065) by a factor of ξ . The modal field radius of LP₀₁ mode at the fiber laser output is calculated to be 8.71 μm [47] and our coupling optics is designed to scale it up to 13 μm by $\xi = 1.5$ at the entrance of AR-HCF which is close to 12.75 μm the radius of the fundamental-like mode.

At 1080 nm the pigtail's normalized frequency V is about 3.782, indicating existence of LP₁₁ modes [48]. Therefore, the incident field can be described by the superposition of LP₀₁ and LP₁₁ modes following [49]

$$E_0(x, y) = \sqrt{1 - \alpha} \cdot E_{01}(x, y) + \sqrt{\alpha} \cdot e^{i\psi} E_{11}(x, y) \quad (3)$$

where $\alpha \in [0, 1]$ is the power fraction factor, and ψ the phase shift between the two superimposed LP modes, which is neglected in the paper for simplification.

To evaluate the maximum coupling efficiency of our experiment in theory, we model our incident beam as a superposition of LP₀₁ and LP₁₁ modes to be coupled with the fundamental and LP₁₁ like HOMs of AR-HCF only. Figures 6(a) and 6(b) show the calculated coupling efficiency as function of the incident beam size and fraction of LP₁₁ mode among the incident beam power, respectively. For the incidence of pure LP₀₁ mode, the highest coupling efficiency 98.46% is achieved when $\xi = 1.5$. As the LP₁₁ mode occupies higher power ratio, the coupling efficiency would be reduced to 97.35% ($\alpha=0.5$) and then 93.62% ($\alpha=1$) when $\xi = 1.5$.

For an 81% coupling efficiency in the experiment, lens fabrication errors/defects, other possible sources of transmission loss, such as excitation of other HOMs of AR-HCF and fiber disuniformity could all considered to contribute to the degraded measured coupling efficiency, requiring more effort in further exploration. It is noted that the measured coupling efficiency was calibrated

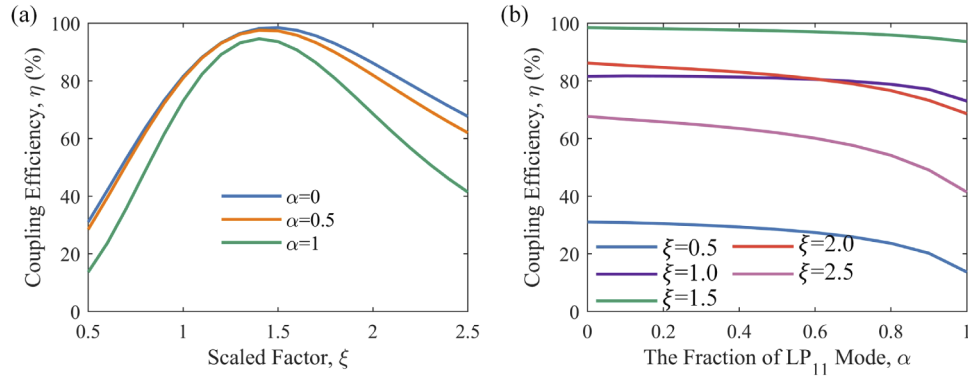


Fig. 6. Calculated coupling efficiency between LP modes of laser beam and modes of AR-HCF (a) for different ξ when α equals 0, 0.5 and 1; (b) for different α as ξ varies from 0.5 to 2.5. Noted that only the fundamental mode and LP_{11} -like modes of AR-HCF are considered.

by the cutback attenuation that was primarily determined by the fundamental-like mode. If we include LP_{11} -like mode of AR-HCF in the calibration and assume its attenuation about 9 times of the measured cutback loss according to our simulation, the maximum coupling efficiency of our experiment may reach as high as 93.5% ($\alpha=0.5$), close to 97.35% as predicted.

4.2. Sensitivity of coupling efficiency on the thermal induced focus change

Laser induced thermal effect could result in lens deformation and change the spatial distribution of refractive index both of which cause the change of focus length accordingly [50]. In our experiment, we measured the laser induced temperature rise of lenses using a thermal imaging camera. When the laser power increases from 0 to 375 W, the temperature of the lens was found to rise from the room temperature to 42°C as shown in Fig. 7(a).

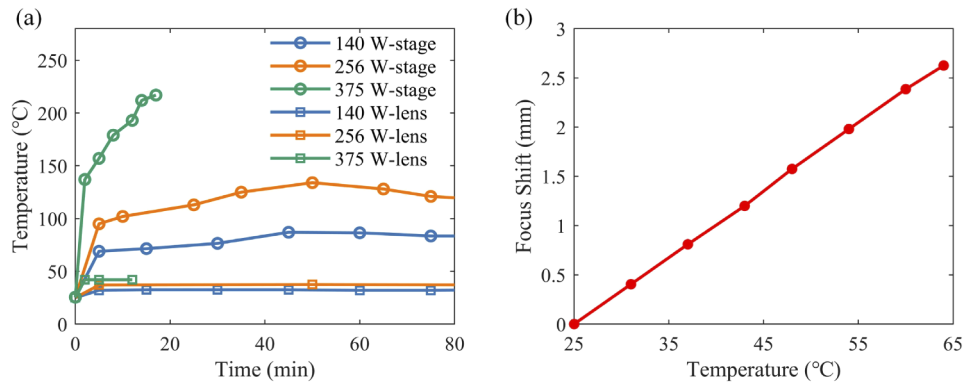


Fig. 7. (a) The temperature of the XYZ stage and lens under different radiation time. The curves with circle represent the temperature of XYZ stage which recorded by adjusting the position of fiber end to stay in the best coupling efficiency. The curves with square represent the temperature of lens (all the lenses are in the same temperature) shown in Fig. 2. Different colors represent different input power; (b) The focus shift of whole system under different temperature of lens.

According to [51], a recognised experimental value of thermal induced focus shift Δf of fused silica lens is around 0.015 mm per 1°C for a single lens. Figure 7(b) presents the simulated focal

length change of our coupling optics at different temperatures by COMSOL. The equivalent focal length of our coupling system is expected to be shortened by 1.1 mm when the temperature of lenses increases to 42°C. Therefore, the manual adjustment of XYZ stage along Z direction is required to compensate. It is noted that the reduced focal length would cause a smaller incident beam size, inevitably degrading the coupling efficiency of AR-HCF.

4.3. On use of XYZ stage

At the incident end of AR-HCF, the leaked laser power not only possibly damages the fiber itself and mount but also heats the XYZ stage giving rise to detrimental mechanical thermal drift which is regarded as the main challenge to the thermal stability of our AR-HCF delivery experiment scheme.

Without any additional cooling the XYZ stage temperature rose up to 217°C under 375 W input power as shown in Fig. 7(b). Figure 8 presents the simulated coupling efficiency as function of the transvers offset Δy of AR-HCF end when the incident beam is assumed as the superposition of LP_{01} and LP_{11} modes ($\alpha = 0.5$). For the optimized beam size when $\xi = 1.5$, the coupling becomes most sensitive to the transverse offset. For a larger incident beam size, the optimized coupling efficiency decreases but also less sensitive to the transverse offset. For a smaller incident beam, it is found that the maximum coupling efficiency appears off $\Delta y = 0$, where a more efficient coupling with LP_{11} -like mode in AR-HCF is expected.

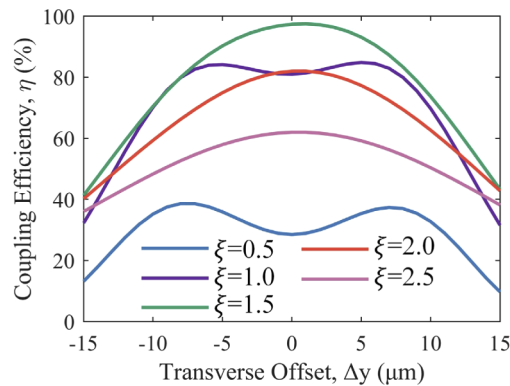


Fig. 8. Calculated the coupling efficiency as function of transverse offset Δy for different incident beam diameter. The incident beam is assumed as superposition of LP_{01} and LP_{11} modes with an equal power ratio ($\alpha = 0.5$)

5. Conclusion

We demonstrate high power CW laser delivery by using uncooled 3 meters AR-HCF at 1080 nm wavelength for several hours' operation. A maximum 300 W power was successfully transmitted without damaging the fiber for operation over hours. Over 10 hours laser delivery test was also demonstrated for a broad range of incident power range without fiber damage. The delivered laser beam at the output end of AR-HCF presents an improved beam quality with a lower M^2 factors than the incident beam. The laser induced thermal effects on both XYZ stages and optics are found to limit the performance of AR-HCF laser delivery and its temporal stability. In the future, both cooling method and new coupling design without XYZ stage will be explored to improve the long-term operation stability of high-power laser delivery by AR-HCF.

Funding. National Natural Science Foundation of China (61935002); Joint International Research Laboratory of Specialty Fiber Optics and Advanced Communication, Shanghai University; Key Research Program of Frontier Sciences, Chinese Academy of Sciences (ZDBS-LY- JSC020); CAS Pioneer Hundred Talents Program.

Disclosures. The authors declare no conflicts of interest.

References

1. U. K. Tirlapur and K. König, "Targeted transfection by femtosecond laser," *Nature* **418**(6895), 290–291 (2002).
2. M. Farsari and B. N. Chichkov, "Two-photon fabrication," *Nat. Photonics* **3**(8), 450–452 (2009).
3. M. Petrarca, S. Henin, N. Berti, M. Matthews, J. Chagas, J. Kasparian, J.-P. Wolf, G. Gatti, G. Di Pirro, M. P. Anania, M. Ferrario, and A. Ghigo, "White-light femtosecond Lidar at 100 TW power level," *Appl. Phys. B* **114**(3), 319–325 (2014).
4. C. Markos, J. C. Travers, A. Abdolvand, B. J. Eggleton, and O. Bang, "Hybrid photonic-crystal fiber," *Rev. Mod. Phys.* **89**(4), 045003 (2017).
5. F. Poletti, M. N. Petrovich, and D. J. Richardson, "Hollow-core photonic bandgap fibers: technology and applications," *Nat. Photonics* **2**(5–6), 315–340 (2013).
6. C. M. Smith, N. Venkataraman, M. T. Gallagher, D. Müller, J. A. West, N. F. Borrelli, D. C. Allan, and K. W. Koch, "Low-loss hollow-core silica/air photonic bandgap fibre," *Nature* **424**(6949), 657–659 (2003).
7. J. D. Shephard, J. D. C. Jones, D. P. Hand, G. Bouwmans, J. C. Knight, and P. St. J. Russell, and B. J. Mangan, "High energy nanosecond laser pulses delivered single-mode through hollow-core PBG fibers," *Opt. Express* **12**(4), 717–723 (2004).
8. M. Michieletto, M. M. Johansen, J. K. Lyngsø, J. Lægsgaard, O. Bang, and T. T. Alkeskjold, "High-power picosecond pulse delivery through hollow core photonic band gap fibers," *Proc. SPIE* **9728**, 97282Z (2016).
9. G. Humbert, J. C. Knight, G. Bouwmans, P. S. J. Russell, D. P. Williams, P. J. Roberts, and B. J. Mangan, "Hollow core photonic crystal fibers for beam delivery," *Opt. Express* **12**(8), 1477–1484 (2004).
10. F. Couny, B. J. Mangan, A. V. Sokolov, and F. Benabid, "High Power 55 Watts CW Raman Fiber-Gas-Laser," in *Conference on Lasers and Electro-Optics 2010*, OSA Technical Digest (CD) (Optical Society of America, 2010), paper CTuM3.
11. D. C. Jones, C. R. Bennett, M. A. Smith, and A. M. Scott, "High-power beam transport through a hollow-core photonic bandgap fiber," *Opt. Lett.* **39**(11), 3122–3125 (2014).
12. Y. Y. Wang, X. Peng, M. Alharbi, C. F. Dutin, T. D. Bradley, F. Gérôme, M. Mielke, T. Booth, and F. Benabid, "Design and fabrication of hollow-core photonic crystal fibers for high-power ultrashort pulse transportation and pulse compression," *Opt. Lett.* **37**(15), 3111–3113 (2012).
13. K. F. Mak, J. C. Travers, N. Y. Joly, A. Abdolvand, and P. S. J. Russell, "Two techniques for temporal pulse compression in gas-filled hollowcore kagomé photonic crystal fiber," *Opt. Lett.* **38**(18), 3592–3595 (2013).
14. F. Emaury, C. F. Dutin, C. J. Saraceno, M. Trant, O. H. Heckl, Y. Y. Wang, C. Schriber, F. Gerome, T. Südmeyer, F. Benabid, and U. Keller, "Beam delivery and pulse compression to sub-50 fs of a modelocked thin-disk laser in a gas-filled kagome-type HC-PCF fiber," *Opt. Express* **21**(4), 4986–4994 (2013).
15. K. Murari, G. J. Stein, H. Cankaya, B. Debord, F. Gérôme, G. Cirmi, O. D. Mücke, P. Li, A. Ruehl, I. Hartl, K.-H. Hong, F. Benabid, and F. X. Kärtner, "Kagome-fiber-based pulse compression of mid-infrared picosecond pulses from a Ho: YLF amplifier," *Optica* **3**(8), 816–822 (2016).
16. F. Emaury, C. J. Saraceno, C. F. Dutin, Y. Y. Wang, C. Schriber, F. Gerome, T. Südmeyer, F. Benabid, and U. Keller, "Efficient femtosecond operation of a Kagome-type HC-PCF fiber at 75 W average power," in *CLEO: 2013*, OSA Technical Digest (online) (Optical Society of America, 2013), paper CTu3 K.1.
17. B. Resan, R. Auchli, V. Villamaina, and R. Holtz, "Dynamic fiber delivery of 3 W 160 fs pulses with photonic crystal hollow core fiber patchcord," *Opt. Express* **25**(20), 24553–24558 (2017).
18. F. Emaury, C. J. Saraceno, B. Debord, D. Ghosh, A. Diebold, F. Gérôme, T. Südmeyer, F. Benabid, and U. Keller, "Efficient spectral broadening in the 100-W average power regime using gas-filled kagome HC-PCF and pulse compression," *Opt. Lett.* **39**(24), 6843–6846 (2014).
19. M. Andreana, T. Le, W. Drexler, and A. Unterhuber, "Ultrashort pulse Kagome hollow-core photonic crystal fiber delivery for nonlinear optical imaging," *Opt. Lett.* **44**(7), 1588 (2019).
20. S. Hädrich, J. Rothhardt, S. Demmler, M. Tschernajew, A. Hoffmann, M. Krebs, A. Liem, O. de Vries, M. Plötner, S. Fabian, T. Schreiber, J. Limpert, and A. Tünnermann, "Scalability of components for kW-level average power few-cycle lasers," *Appl. Opt.* **55**(7), 1636–1640 (2016).
21. Y. Y. Wang, N. V. Wheeler, F. Couny, P. J. Roberts, and F. Benabid, "Low loss broadband transmission in hypocycloid-core Kagome hollow-core photonic crystal fiber," *Opt. Lett.* **36**(5), 669–671 (2011).
22. A. D. Pryamikov, A. S. Biriukov, A. F. Kosolapov, V. G. Plotnichenko, S. L. Semjonov, and E. M. Dianov, "Demonstration of a waveguide regime for a silica hollow - core microstructured optical fiber with a negative curvature of the core boundary in the spectral region $> 3.5 \mu\text{m}$," *Opt. Express* **19**(2), 1441–1448 (2011).
23. F. Yu and J. C. Knight, "Spectral attenuation limits of silica hollow core negative curvature fiber," *Opt. Express* **21**(18), 21466–21471 (2013).
24. F. Yu and J. C. Knight, "Negative Curvature Hollow-Core Optical Fiber," *IEEE J. Sel. Top. Quantum Electron.* **22**(2), 146–155 (2016).
25. G. T. Jasion, T. D. Bradley, H. Sakr, J. R. Hayes, Y. Chen, A. Taranta, H. C. H. Mulvad, I. A. Davidson, N. V. Wheeler, E. R. Numkam Fokoua, W. Wang, D. J. Ricardson, and F. Poletti, "Recent breakthroughs in hollow core fiber technology," *Proc. SPIE* **11309**, 1 (2020).
26. F. Poletti, "Nested antiresonant nodeless hollow core fiber," *Opt. Express* **22**(20), 1 (2014).

27. W. Belardi and J. C. Knight, "Hollow antiresonant fibers with reduced attenuation," *Opt. Lett.* **39**(7), 1853 (2014).
28. M. S. Habib, J. E. Antonio-Lopez, C. Markos, A. Schülzgen, and R. Amezcua-Correa, "Single-mode, low loss hollow-core anti-resonant fiber designs," *Opt. Express* **27**(4), 3824–3836 (2019).
29. P. Uebel, M. C. Günendi, M. H. Frosz, G. Ahmed, N. N. Edavalath, J.-M. Ménard, and P. S. J. Russell, "Broadband robustly single-mode hollow-core PCF by resonant filtering of higher-order modes," *Opt. Lett.* **41**(9), 1961–1964 (2016).
30. F. Yu, P. Song, D. Wu, T. Birks, D. Bird, and J. Knight, "Attenuation limit of silica-based hollow-core fiber at mid-IR wavelengths," *APL Photonics* **4**(8), 080803 (2019).
31. D. Wu, F. Yu, and M. Liao, "Understanding the material loss of anti-resonant hollow-core fibers," *Opt. Express* **28**(8), 11840–11851 (2020).
32. R. M. Carter, F. Yu, W. J. Wadsworth, J. D. Shephard, T. Birks, J. C. Knight, and D. P. Hand, "Measurement of resonant bend loss in anti-resonant hollow core optical fiber," *Opt. Express* **25**(17), 20612–20621 (2017).
33. P. Jaworski, F. Yu, D. G. MacLachlan, R. R. J. Maier, R. R. Thomson, W. J. Wadsworth, J. C. Knight, J. D. Shephard, and D. P. Hand, "A hollow-core Negative Curvature Fibre for efficient delivery of NIR picosecond and femtosecond pulses for precision micro-machining," in *Workshop on Specialty Optical Fibers and their Applications*, (Optical Society of America, 2013), paper F3.3.
34. Y. Chen, Z. Wang, B. Gu, F. Yu, and Q. Lu, "Achieving a 1.5 μm fiber gas Raman laser source with about 400 kW of peak power and a 6.3 GHz linewidth," *Opt. Lett.* **41**(21), 5118–5121 (2016).
35. Z. Wang, Y. Chen, B. Gu, F. Yu, and C. Zhang, "About 400 kW Peak-Power, 7.5 GHz Linewidth, 1.5 μm Fiber Gas Raman Source," in *Lasers Congress 2016 (ASSL, LSC, LAC)*, OSA Technical Digest (online) (Optical Society of America, 2016), paper JTu2A.13.
36. A. N. Kolyadin, G. K. Alagashev, A. D. Pryamikov, L. Mouradian, A. Zeytunyan, H. Toneyan, A. F. Kosolapov, and I. A. Bufetov, "Negative Curvature Hollow-core Fibers: Dispersion Properties and Femtosecond Pulse Delivery," *Phys. Procedia* **73**, 59–66 (2015).
37. B. Sherlock, F. Yu, J. Stone, S. Warren, C. Paterson, M. A. A. Neil, P. M. W. French, J. Knight, and C. Dunsby, "Tunable fibre-coupled multiphoton microscopy with a negative curvature fiber," *J. Biophotonics* **9**(7), 715–720 (2016).
38. P. Jaworski, F. Yu, R. R. J. Maier, W. J. Wadsworth, J. C. Knight, J. D. Shephard, and D. P. Hand, "Picosecond and nanosecond pulse delivery through a hollow-core negative curvature fiber for micro-machining applications," *Opt. Express* **21**(19), 22742–22753 (2013).
39. S. Eilzer and B. Wedel, "Hollow Core Optical Fibers for Industrial Ultra Short Pulse Laser Beam Delivery Applications," *Fibers* **6**(4), 80 (2018).
40. P. Jaworski, F. Yu, R. M. Carter, J. C. Knight, J. D. Shephard, and D. P. Hand, "High energy green nanosecond and picosecond pulse delivery through a negative curvature fiber for precision micro-machining," *Opt. Express* **23**(7), 8498–8506 (2015).
41. M. Michieletto, J. K. Lyngsø, C. Jakobsen, J. Lægsgaard, O. Bang, and T. T. Alkeskjold, "Hollow-core fibers for high power pulse delivery," *Opt. Express* **24**(7), 7103–7119 (2016).
42. F. Yu, M. Cann, A. Brunton, W. Wadsworth, and J. Knight, "Single-mode solarization-free hollow-core fiber for ultraviolet pulse delivery," *Opt. Express* **26**(8), 10879–10887 (2018).
43. S.-F. Gao, Y.-Y. Wang, W. Ding, and P. Wang, "Hollow-core negative-curvature fiber for UV guidance," *Opt. Lett.* **43**(6), 1347–1350 (2018).
44. F. Yu, M. Xu, and J. C. Knight, "Experimental study of low-loss single-mode performance in anti-resonant hollow-core fibers," *Opt. Express* **24**(12), 12969–12975 (2016).
45. P. Song, K. Y. Phoong, and D. Bird, "Quantitative analysis of anti-resonance in single-ring, hollow-core fibres," *Opt. Express* **27**(20), 27745–27760 (2019).
46. P. J. Winzer and W. R. Leeb, "Fiber coupling efficiency for random light and its applications to lidar," *Opt. Lett.* **23**(13), 986–988 (1998).
47. D. Marcuse, "Loss Analysis of Single-Mode Fiber Splices," *Bell Syst. Tech. J.* **56**(5), 703–718 (1977).
48. D. Gloge, "Weakly guiding fibers," *Appl. Opt.* **10**(10), 2252–2258 (1971).
49. H. Yoda, P. Polynkin, and M. Mansuripur, "Beam quality factor of higher order modes in a step-index fiber," *J. Lightwave Technol.* **24**(3), 1350–1355 (2006).
50. S. Faas, D. J. Foerster, R. Weber, and T. Graf, "Determination of the thermally induced focal shift of processing optics for ultrafast lasers with average powers of up to 525 W," *Opt. Express* **26**(20), 26020–26029 (2018).
51. X. Z. Liu, L. N. Liu, and J. B. Zhou, "Simulated and experimental study on temperature induced lens focal shifts," *Optoelectron. Lett.* **15**(4), 245–249 (2019).